SAND2022-3812J

Fault Current Control and Protection in a Standalone DC Microgrid Using Adaptive Droop and Current Derivative

Sijo Augustine[1], Matthew J. Reno[2], Sukumar M. Brahma[3], and Olga Lavrova[1]

[1] Klipsch School of Electrical Computer Engineering, New Mexico State University, USA
[2]Electric Power Systems Research, Sandia National Laboratories, USA
[3]Holcombe Department of Electrical Computer Engineering, Clemson University, USA

***Abstract*—This paper presents a novel fault detection, characterization, and fault current control algorithm for a standalone solar-photovoltaic (PV) based DC microgrids. The protection scheme is based on the current derivative algorithm. The over-current and current directional/differential comparison based protection schemes are incorporated for the DC microgrid fault characterization. For a low impedance fault, the fault current is controlled based on the current/voltage thresholds and current direction. Generally, the droop method is used to control the power-sharing between the converters by controlling the reference voltage. In this paper, an adaptive droop scheme is also proposed to control the fault current by calculating a virtual resistance R_{droop}, and to control the converter output reference voltage. For a high impedance fault, differential comparison method is used to characterize the fault. These algorithms effectively control the converter pulse width and reduce the flow of source current from a particular converter, which helps to increase the fault clearing time. Additionally, a trip signal is sent to the corresponding DC circuit breaker (DCCB), to isolate the faulted converter, feeder or a DC bus. The DC microgrid protection design procedure is detailed, and the performance of the proposed method is verified by simulation analysis.**

Keywords: Current derivative, DC Microgrid, directional protection, differential protection, droop control, fault current, islanded, low voltage, protection, solar-PV, voltage control.

I. Introduction

DC microgrids are emerging as an attractive solution allowing customers to maintain electrical service independent of the main grid. In terms of size, a microgrid covers a small geographical area, and the distribution line length is short compared to conventional AC distribution systems [1], [2]. One major concern related to the smooth operation and control of DC microgrids is protection [3], [4]. Based on the system components and topology, faults in a solar-PV based DC microgrid system are classified as either short circuit line-line (L-L) and line-ground (L-G)) or PV arc faults [5], [6] as shown in Fig. 1.

Due to the low impedance nature of DC microgrid system, the capacitive filters associated with the converters will rapidly discharge into a fault, resulting in large current surges within a very short duration. This may lead to an unstable operation of the system or even damage the converters if the fault is not isolated from the system [7], [8]. Therefore, the severity and magnitude of fault current is high if a low impedance fault occurs in DC microgrid systems. Also damage due to arcing and difficult to extinguish without zero crossings.

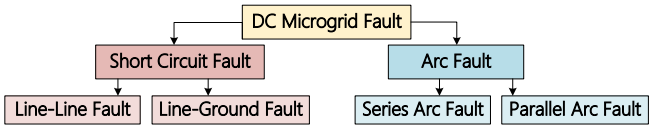

Fig. 1. Classification of solar-PV DC microgrid fault.

One of the main challenges associated with the DC microgrid protection is lack of standards and guidelines. The recent development in standards and guidelines are discussed in [8]. D. S. Pillai et. al [9] conducted a detailed compatibility analysis on NEC, IEC, and UL standards for fault protection in PV arrays and some of these standards can be adapted to DC microgrid protection scenario. The DC microgrid fault current magnitude is a function of the type of renewable energy sources, magnitude of DC bus voltage, bus capacitors, type of fault, location, fault impedance, type of grounding, topology of the converters, and the control schemes. During L-G faults, the magnitude of the fault current depends on the DC bus voltage, DC microgrid grounding [10]–[12], and system topology. Therefore, to design a good DC microgrid protection scheme, it is necessary to identify, characterize and clear the fault in the minimum time possible.

[4], [7], [8], [13]–[15] discuss the common DC microgrid fault detection methods like current/voltage magnitude, rate of current rise, differential current, oscillation frequency, power probe based non-unit protection, wavelet transform, artificial intelligence, etc. As discussed in [5], [8], [16]–[23], a widely used and cost effective method for microgrid protection involves using voltage and current thresholds. For example, when a fault occurs, there is a drop in the bus voltage and a rise in the converter current. These changes are used to generate a trip signal by comparing the magnitudes of these signals to some predefined thresholds. This method relies solely on current and voltage magnitudes, allowing for fast fault detection. Current derivative based protection is discussed in [24]. This paper proposes rate-of-rise protection based on the change in current and its slope characteristics, but no discussion about setting the current derivative threshold. Karthik

et.al [25] discussed a residential DC microgrid protection using solid state CB (SSCB). SSCB performance and characteristics are evaluated in detail for 340 V DC residential microgrid systems. A current differential protection scheme based on synchronization of current measurements and comparison is proposed in [26]. This method gives a good performance when a L-L fault occurs, and it does not characterize the fault based on the fault type or disturbances. A short-duration spread frequency current spike active impedance estimation method is proposed [20], [21]. The accuracy of this method may vary with the sensing parameters and mathematical formulations derived to estimate the location. A power probe based DC microgrid fault detection scheme is proposed in [22] uses a power source, capacitor, inductor and CB's to locate and clear the fault. A combination of voltage and current derivative-based fault detection scheme is described in [23]. This method uses the current direction, rate of change of currents, and rate of change of voltages information to detect the fault. This helps to classify the faults as internal or external. For example, during a cable fault, a positive current derivative shows the fault is within the protection zone, and a negative current derivative indicates an external fault. Difficulty in classifying load changes, transients, and faults is the main drawback of this algorithm.

In [12], the authors analyzed the performance of a DC microgrid system with a droop based protection scheme. In this paper, the authors extended the previous work with an improved fault detection, characterization, and current control. The proposed method uses the rate of rise of current, directional/differential current comparison, and an adaptive droop method to detect and isolate the fault. The proposed concept is explained based on a 4-bus DC microgrid, and the system configuration is discussed in Section II. Section III details the proposed algorithm along with the flowchart. Simulation results are presented in Section IV and finally, conclusions are summarized in Section V.

II. System Configuration and Fault Characterization

A standalone 4-bus DC microgrid system incorporated with PV systems and battery based energy storage device is shown in Fig. 2. Each bus consists of two parallel connected solar-PV boost converters, one bidirectional converter for energy storage, and DC loads. A detailed connection of converters and fault locations at bus#1 is shown in Fig. 3(a). Where V_{DC1}, V_{DC2}, V_{B1}, I_{pv1}, I_{pv2}, and I_{B1}, represent the output voltages, and currents of converter-1, converter-2 and bidirectional converter-1. $R_{pv1}\&L_{pv1}$, $R_{pv2}\&L_{pv2}$, and $R_{B1}\&L_{B1}$ represent the cable resistance & inductance and Z_{L12}, Z_{L23}, Z_{L43}, and Z_{L14} are the cable impedances between the DC buses. Also, the individual converter power at any instant is represented as P_{pv1}, P_{pv2} and P_{B1}. F_1 and F_2 are the low impedance L-L fault locations and F_3 is the high impedance L-G fault considered in the system. The bus#1 control parameters, and the point of measurements are given in Table I. These parameters are measured and controlled using an Intelligent Electronic Devices (IED) with a centralized controller. An assumption considered in this paper is that the centralized controller and the local controllers will coordinate and analyze the measured parameters with minimum time to effectively detect and isolate the fault.

The equivalent circuit of bus#1 during a fault is shown in Fig. 3(b). If a L-L (F_1) or L-G (F_3) occurs at converter-1 as shown in Fig. 3(a), the total fault current can be calculated as,

$$i_f = i_{f,pv1} + i_{f,pv2} + i_{f,B1} + i_{f,Bus\#2} + i_{f,Bus\#4}, \quad (1)$$

where,

$$|i_{f,pv1}| > |i_{f,pv2}|, |i_{f,B1}|, |i_{f,Bus\#2}|, |i_{f,Bus\#4}|.$$

Converter-1's contribution to the fault current can be divided into two components [13]: (i) the fault current component from the DC power source and (ii) the current from the DC bus capacitor. The fault current component from the solar-PV source is,

$$i_{f,pv1_{PV}}(t) = \frac{V_{pv}}{R_{eq}}\left[1 - e^{\left[\frac{-t}{\tau_1}\right]}\right], \quad (3)$$

where, τ_1 is the time constant of the converter-1 source fault current and depends on the line reactance. Similarly, the capacitor component can be expressed as,

$$i_{f,pv1_{Capa}}(t) = \frac{V_C}{R_{ESR}}\left[e^{\left[\frac{-t}{\tau_2}\right]}\right], \quad (4)$$

where, τ_2 is the time constant of the converter-1 capacitor fault current component and depends on the equivalent series resistance (ESR) and capacitance of the DC bus capacitor. It should be noted that due to the small scale of the time constant, the component of the fault current due to the DC capacitor can rapidly ramp to relatively large magnitudes. Converter-1 fault current contribution during F_1 is shown in Fig. 4. It is observed that within 20 μs, the converter-1 fault current reaches a maximum of approximately 50 A, and the capacitor current contribution is approximately 40 A.

From the above discussions, it can be concluded that the source component and the capacitor component should be controlled for the safe operation of the converter during the fault. Also, the fault current magnitude may vary because of the low impedance of the DC cables. To address these issues, the proposed method is introduced in the next section.

III. Proposed Algorithm

The proposed fault current control algorithm combines a $\frac{di}{dt}$ method for fault detection, a directional and differential comparison method for fault characterization and an adaptive droop control technique for controlling the source current. The fault detection based on the $\frac{di}{dt}$ will help to differentiate the DC microgrid system events. This is achieved by setting the $\frac{di}{dt}$ threshold ($\frac{di}{dt}_{(th)}$). A major problem associated with the $\frac{di}{dt}$ method is that in a multi-converter/multi-bus DC microgrid system, due to the low impedance of the DC cables and system topology, false triggering may occur in multiple converters based on the selected $\frac{di}{dt}_{(th)}$. For example, during F_1, due to the low cable impedance, the converter-2 algorithm

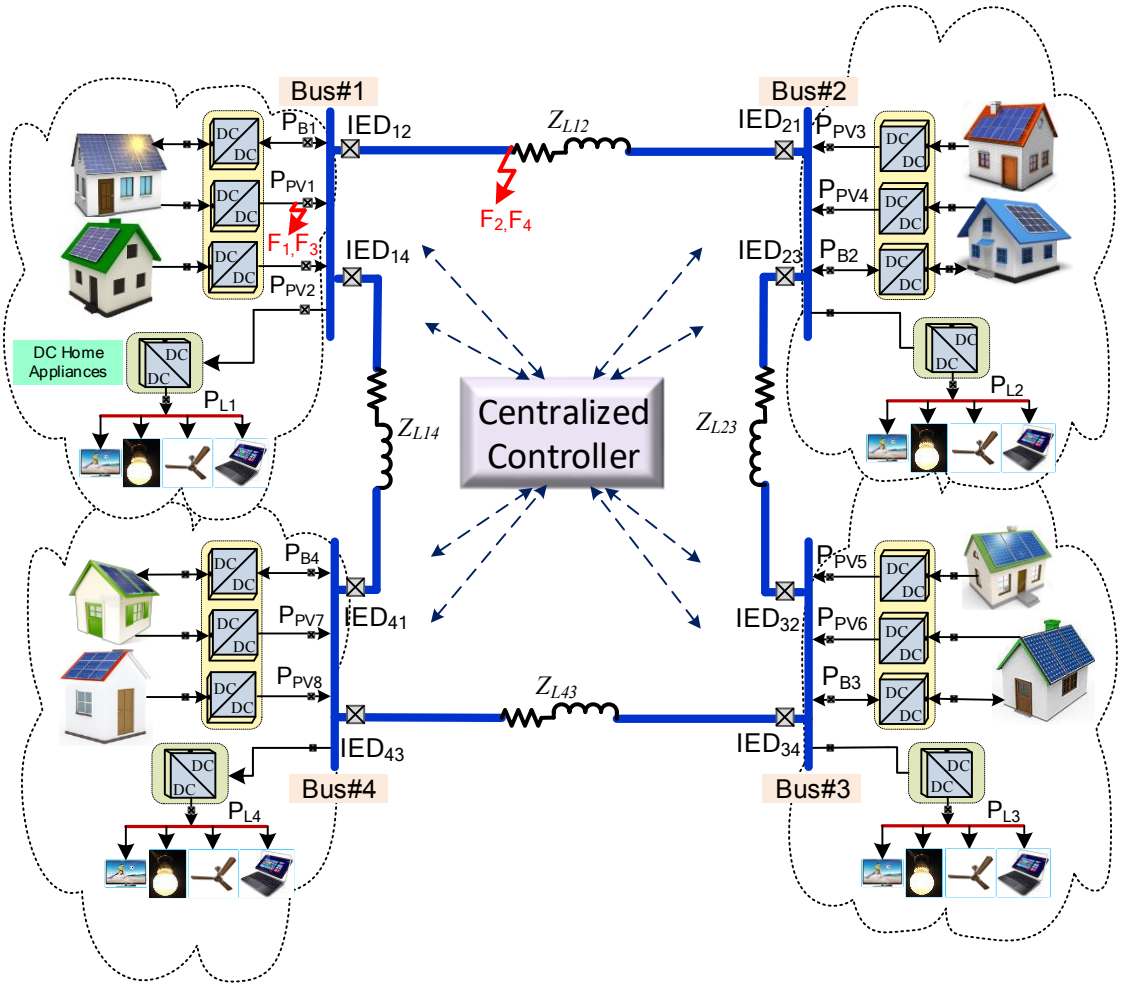

Fig. 2. Schematic representation of a 4-bus DC microgrid system.

TABLE I
DC BUS#1 CONTROL PARAMETERS AND POINT OF MEASUREMENTS

Component	**Source side**	**Converter side**		**bus#1 side** (IED_x)		**Feeder** (IED_{xy})		
			$\frac{di}{dt}$ **Directional/ Differential comparison**			$\frac{di}{dt}$ **Directional/ Differential comparison**		
Converter-1 (PV1)	S_1	$V_{DC1},\ I_1$	I_{pv1}	$I_{pv1@IED_1}$	$V_{bus\#1}$	-	-	-
Converter-2 (PV2)	S_2	$V_{DC2},\ I_2$	I_{pv2}	$I_{pv2@IED_2}$		-	-	-
Bi-directional Converter-1 (B1)	SOC_{B1}	$V_{B1},\ I_{batt}$	I_{B1}	$I_{B1@IED_3}$		-	-	-
bus#1-bus#2 Feeder	-	-	-	-	-	$I_{bus_{12}}$	$I_{bus_{21}}$	$V_{bus\#1}$
bus#1-bus#4 Feeder	-	-	-	-	-	$I_{bus_{14}}$	$I_{bus_{41}}$	$V_{bus\#2}$ $V_{bus\#4}$

may generate a trip signal based on the $\frac{di}{dt}_{(th)}$. Also a high impedance ground faults like human body faults, tree touching etc. may be difficult to identify because of the low fault current, or sometimes it may be treated as a large load change based on the $\frac{di}{dt}$. The $\frac{di}{dt}_{(th)}$ gradient for different system events are shown in Fig. 5. The $\frac{di}{dt}_{(th)}$ gradient for low impedance fault with different fault resistances are shown in Fig. 5(a, b). Fig. 5(c, d) represents the high impedance faults and large load changes respectively. Finally, Fig. 5(e) indicates $\frac{di}{dt}_{(th)}$ gradient for a small load change/disturbances. Based on these values, Fig. 6 shows different zones for the DC microgrid fault characterization based on a system event like load change or faults. Accurate classification of events is difficult due to the overlapping zones based on the $\frac{di}{dt}$ magnitude. The threshold is calculated by considering the $\frac{di}{dt}$ value for a 'maximum allowable step change in load' for a particular converter, and hence, the Zone#2 and Zone#3 will be treated as fault zones for the safe operation of the DC microgrid system. Also, due to the low impedance of the DC cables, a fault in the Converter-1 cable may be identified as Converter-2 fault. Therefore, to avoid false triggering of the CB's, it is necessary to add a fault characterization algorithm.

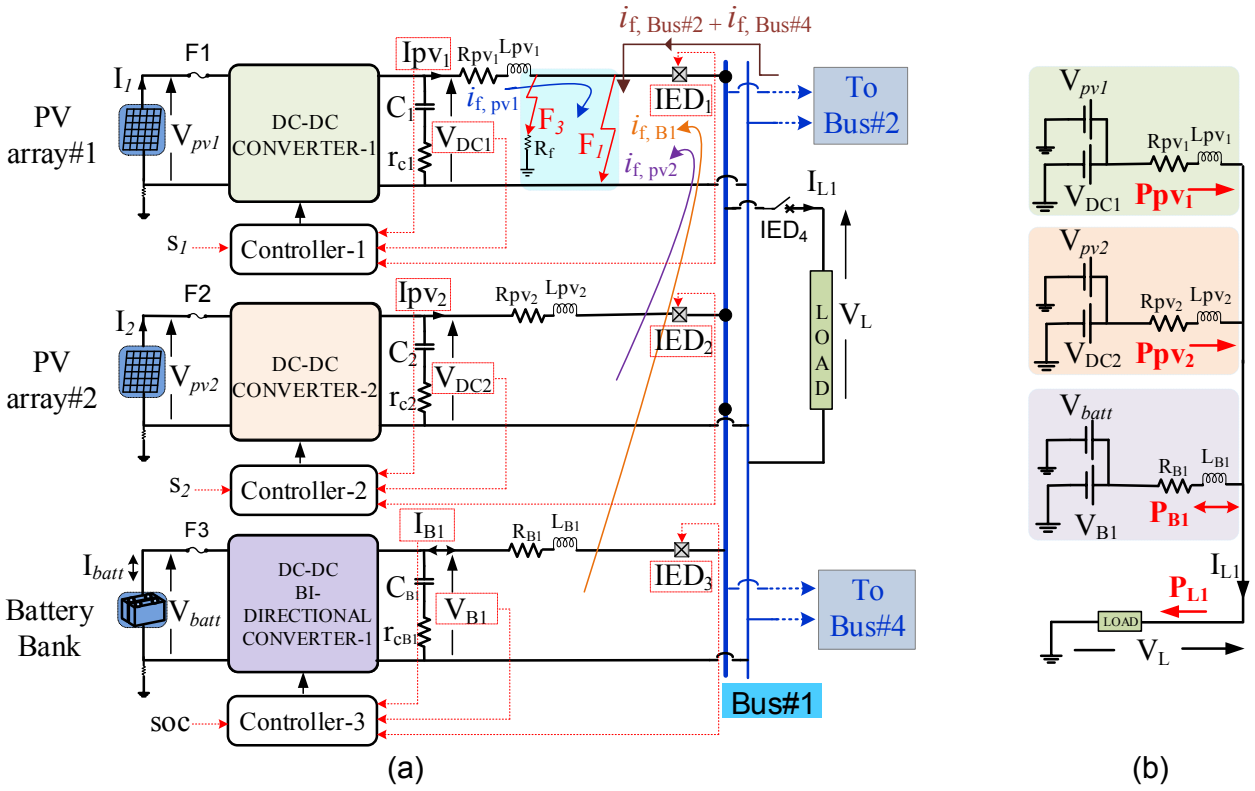

Fig. 3. (a) Detailed schematic representation of bus#1 with a L-L cable fault and L-G fault and (b) Steady state equivalent circuit.

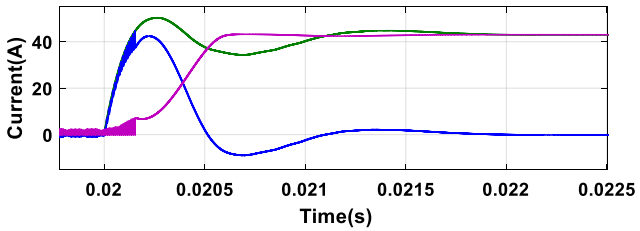

Fig. 4. Fault current contribution of converter-1 during F_1. [Blue → Capacitor Current, Violet→ Source Current, and Green→ Output Current]

In the proposed algorithm, the measured voltage and current signals are filtered to remove all the unwanted frequency components to get an accurate result and to avoid false triggering. This resultant signals can be used to characterize the faults in the DC microgrid as shown in Fig. 7. Based on the $\frac{di}{dt}(th)$, the large load disturbances are also considered as faults but can be characterized by using the directional and differential current comparison. Therefore, an adaptive droop based over-current protection with directional comparison for low impedance faults and differential comparison based protection for high impedance faults are incorporated in the proposed algorithm.

In a DC microgrid system, one of the best way to limit the fault current is controlling the converter/source current. In the droop method, for the desired power sharing, the converters' output voltages and input currents can be controlled by adjusting the reference voltage of each converter. This idea can be extended for controlling the converter fault current. In order to achieve this, during fault conditions, the reference voltage of each converter is controlled by using the virtual impedance R_{droop} [27] shown in Fig. 8. The adjustments in the reference voltage is made by taking the output current feedback from the converter multiplied with the calculated R_{droop}. This resultant signal is subtracted from the reference voltage (V^*_{DC}) of the converter, and the new reference signal is now (V^{**}_{DCj}) and is given as,

$$V^{**}_{DCj} = V^*_{DC} - i_j \times (\pm R_{droop_j}). \quad (5)$$

The algorithm is discussed as follows, and the flowchart is given in Fig. 9.

A. Low Impedance Fault (Line-Line)

The low impedance fault can be controlled based on the voltage and current thresholds. Using the proposed adaptive droop protection method, the output converter voltage is controlled during the fault to avoid complete shutdown of the DC microgrid during the fault. This can be explained with Fig. 2. In the considered system, each bus consists of six IED's and all converters and loads can be isolated based on the fault location. The proposed protection scheme for low impedance fault is discussed below.

1) The first step is to calculate the current and voltage thresholds based on the converter rating, DC bus voltage limits, and load parameters. In the proposed method, the current thresholds are based on converter current rating, topology, and voltage thresholds defined by the allowable limits of DC grid voltage. These current thresholds are selected by considering the converter

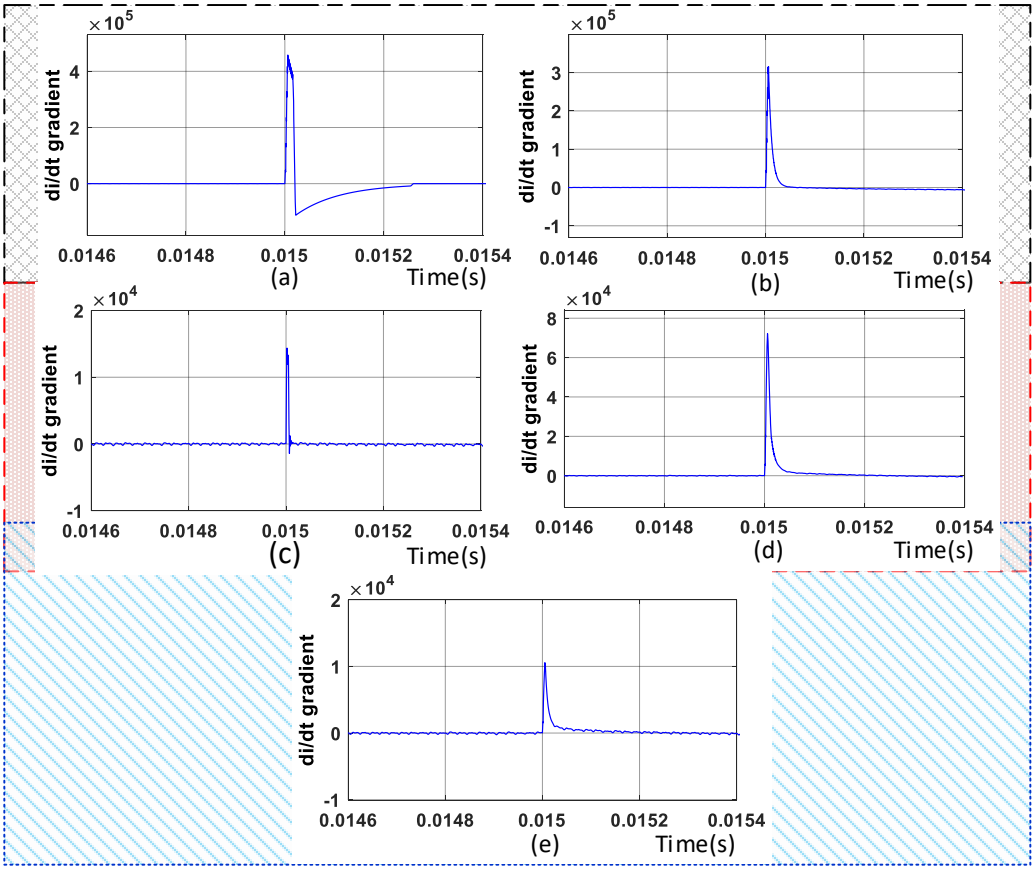

Fig. 5. $\frac{di}{dt}$ gradient measured for Converter-1 faults and bus#1 load change (a) 1Ω line-line fault (F_1) (b) 10Ω line-line fault (F_1) (c) 500Ω line-ground fault (F_3) (d) Load change from 3 A to 8 A, and (e) Load change from 3 A to 4 A.

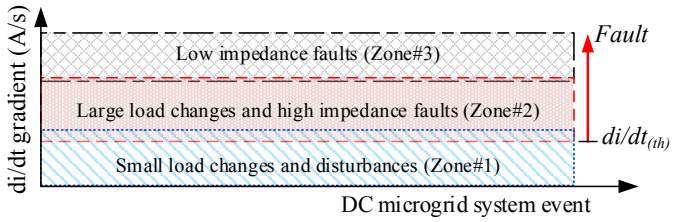

Fig. 6. Classification of system events based on $\frac{di}{dt}$ gradient.

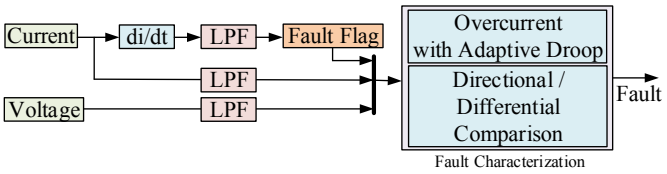

Fig. 7. Proposed DC microgrid fault characterization.

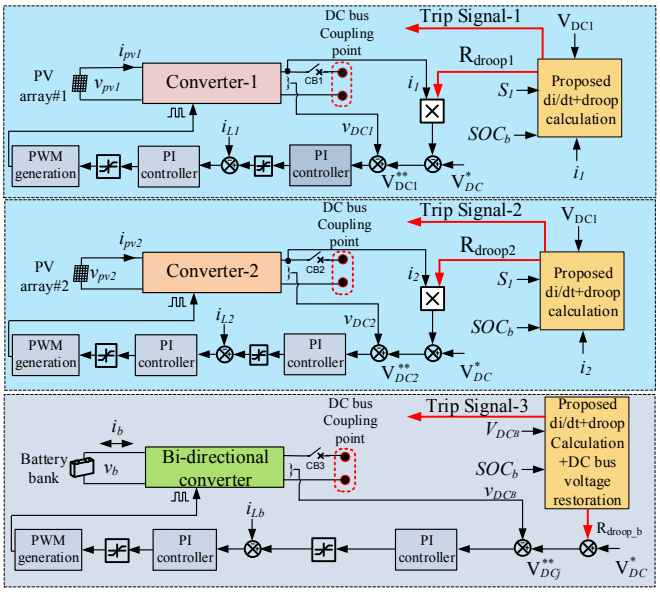

Fig. 8. Control diagram of bus#1 converters with the proposed algorithm.

input current, device (MOSFET or IGBT) current, or the output current. If the current or voltage magnitude crosses the threshold, the controller activates the proposed algorithm.

2) There are two current thresholds and two voltage thresholds, an upper threshold (UT_I & UT_V) and a lower threshold (LT_I & LT_V) as shown in Fig. 10. For example, the upper current threshold can be selected as 150% of the full load current, and the lower threshold as 120% of the full load value. Similarly, the voltage thresholds are based on the allowable DC bus voltage deviation. If the DC bus voltage is 48 V, then the thresholds

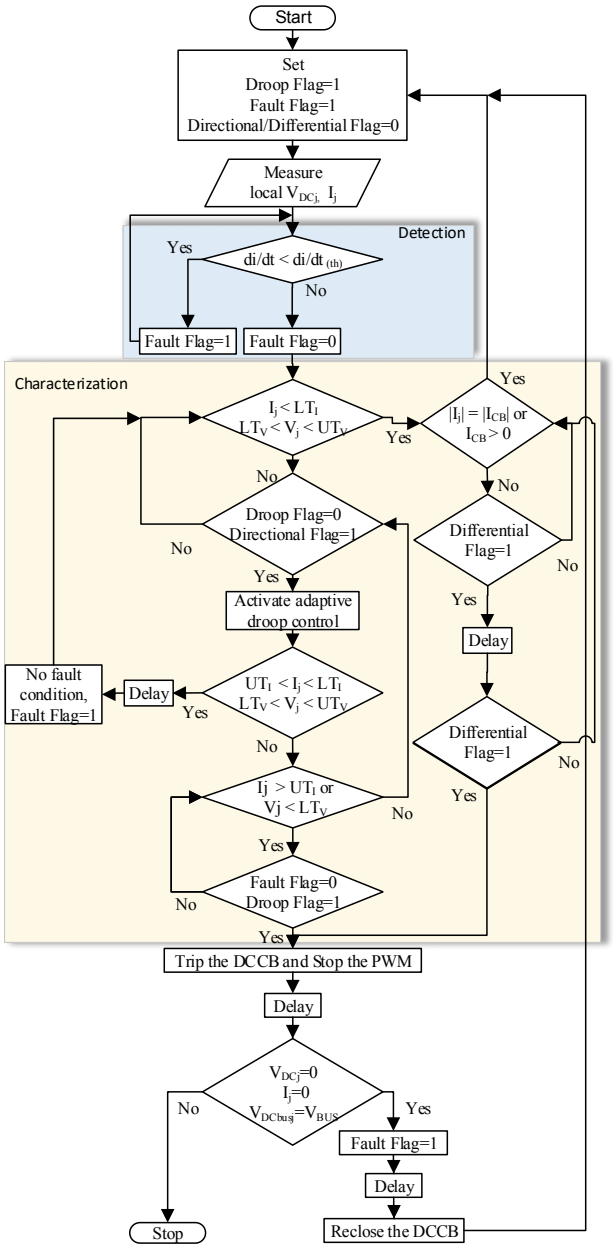

Fig. 9. Flowchart for converter-j $(j = 1, 2..n)$ fault protection algorithm.

can be selected as $48 \pm 2.5\% V$ (lower threshold) and $48 \pm 20\% V$(upper threshold). It should be noted that a small change in the converter output voltage will affect the current sharing proportion among the converters.

3) The proposed method is activated only if the current or voltage magnitude crosses lower threshold as shown in Fig. 10. The control algorithm adjusts the converter output voltage and reduces the total converter output current. If the current again exceeds the threshold UT_I, then the algorithm detects it as a low impedance fault and will send a trip signal to the particular DCCB.
4) During a fault, if the current measured from the converter is less than the threshold, then the current direction comparison algorithm will generate a trip signal to corresponding DCCB.

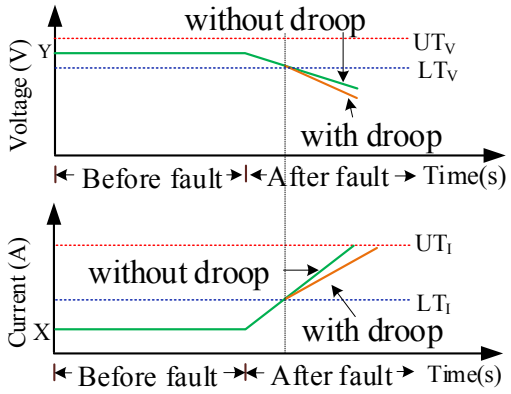

Fig. 10. Voltage and current profile of converter-j $(j = 1, 2..n)$ with and without adaptive droop algorithm.

B. High Impedance Fault (Line-Ground)

During the operation of the DC microgrid, there may be chances for the human-body faults. In this case, due to the high body resistance, the fault current will be typically very low. Therefore, identifying a high impedance fault is difficult because the current magnitude is always much smaller than the threshold and there won't be any change in the current direction. In this paper a high impedance fault F_3, as shown in Fig. 3 is characterized using the differential current comparison based protection algorithm. The algorithm uses the difference in the measured branch current for characterizing the high impedance fault as shown in Fig. 7. This can be explained as follows. In the considered system, the PV converter current direction is always from source to load and the bidirectional converter (battery) current direction can be positive or negative based on the charging/discharging condition. Therefore, the current differential comparison scheme will activate if the differential current is greater than 50 mA threshold. There is an additional time delay of t s (in this paper t=1 ms) is given to trip the CB. This delay is is provided to make sure that the high impedance fault is not a temporary fault. The CT's, associated with the converter and at the DC bus end (IED_x (where, x=1,2,3..) in Fig. 3) are the points of measurement for the differential comparison. If the calculated $\frac{di}{dt}$ is above the $\frac{di}{dt}(th)$, the algorithm will distinguish the large load changes and a high impedance fault.

IV. Simulation Studies

The DC microgrid system as shown in the Fig. 2 was simulated, using MATLAB/Simulink. The system parameters are given in the Table II. The proposed control schemes are implemented, and the voltage, current and $\frac{di}{dt}(th)$ thresholds are defined in Table III.

A. Low Impedance Fault

1) Converter-Bus Cable Fault (F_1): At 0.02 s a line-line fault with a fault resistance, R_f=1 Ω is created in the converter-1 to bus#1 cable as shown in Fig. 3. The corresponding simulation results are shown in Fig. 11. In Fig. 11(a) it can be observed that, the measured $\frac{di}{dt}$ of the converter-1 is

TABLE II
NOMINAL SYSTEM PARAMETERS

Parameters	Symbol	Value
DC bus voltage	V_{DC}	48 V
Boost converter power	P_{boost}	240 W
Battery converter power	P_{batt}	240 W
Cable resistance	R_{cable}	0.01 Ω
Filter inductor	L	100 μH
ESR of filter inductor	r_L	0.03 Ω
Filter capacitor	C	440 μF
ESR of filter capacitor	r_C	0.05 Ω
Nominal switching frequency	f_{sw}	10 kHz
Fault resistance	R_f	1-500 Ω

TABLE III
THRESHOLDS

Parameter	Magnitude
Voltage	UT_V = 46 V LT_V = 35 V
Current	UT_I = 10 A LT_I = 6 A
$\frac{di}{dt}_{(th)}$	1×10^4 A/s

greater than the other converter's $\frac{di}{dt}$. Therefore, a fault is detected at the converter-1, and trip signal is sent to isolate the converter when the current reaches 10 A threshold as shown in Fig. 11(c). Fig. 11(d, e) shows the fault flag, and calculated adaptive droop respectively. The corresponding bus voltages, and currents are shown in Fig. 12. The bus#4, and bus#2 fault current contribution is evident from Fig. 12(b), and it can be seen that bus#4 is sharing the major portion of the fault current.

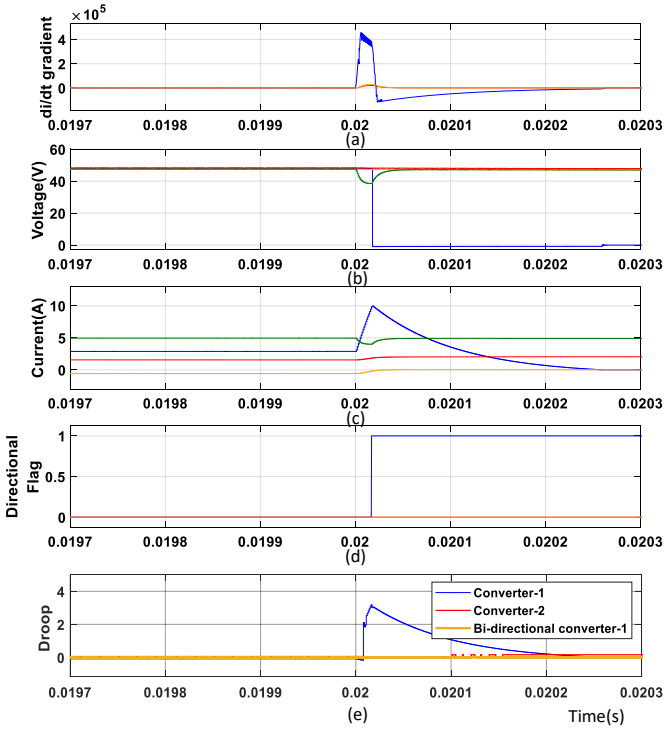

Fig. 11. Bus#1 converter's results for L-L fault F_1 with R_f=1 Ω at 0.02 s (a) di/dt gradients (b) Output voltages (c) Output currents (d) Directional flags, and (e) Calculated adaptive droop values. [Blue → Converter-1, Red→ Converter-2, Yellow→ Bi-directional Converter, and Green→ Load Current]

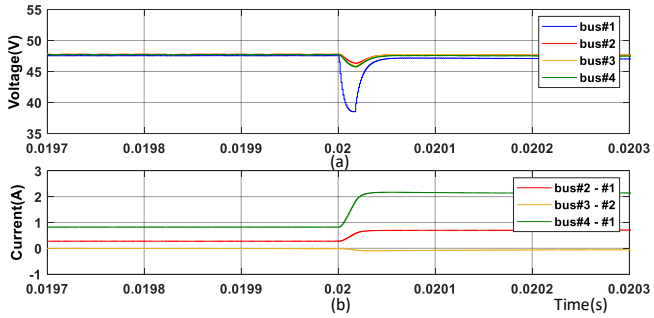

Fig. 12. Results for L-L fault F_1 with R_f=1 Ω at 0.02 s (a) Bus voltages, and (b) Bus currents

As discussed in the Section II, 10 A is selected as the source current threshold instead of converter-1 output current threshold. The results without utilizing the proposed control algorithm are shown in Fig. 13(a, b). In this case the total time taken to clear the fault is approximately 205 μs as shown in Fig. 13(b). Fig. 14(a, b) shows the fault clearing time with the proposed adaptive droop control. The droop adjusts the source current, and hence it gives an additional time to reach the threshold. In this case the total time taken by the fault current to cross the threshold is approximately 265 μs. From the above results and discussions, it can be concluded that with the proposed algorithm an additional 60 μs is available to clear the fault.

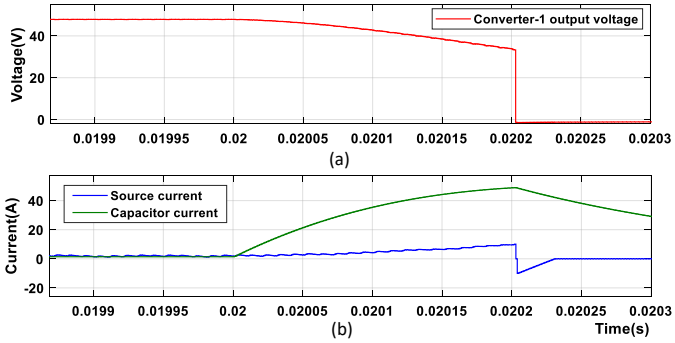

Fig. 13. Converter-1 results for fault F_1 at 0.02 s without proposed algorithm (a) Output voltage (b) Source and capacitor currents.

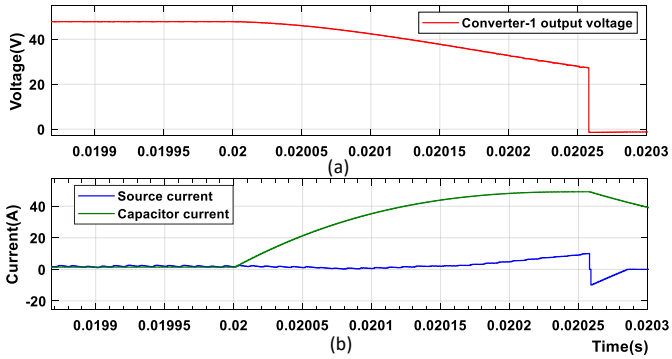

Fig. 14. Converter-1 results for fault F_1 at 0.02 s at 0.02 s with proposed algorithm (a) Output voltage, and (b) Source and capacitor currents.

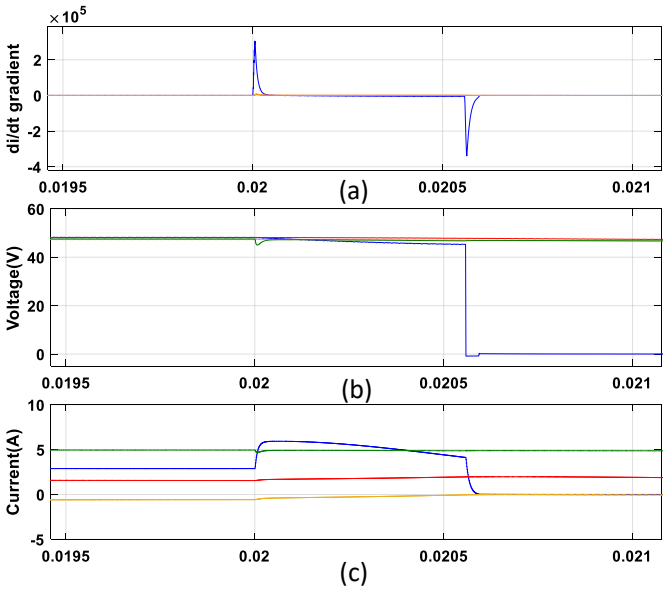

Fig. 15. Bus#1 converter's results for L-L fault (F_1) with R_f=10 Ω at 0.02 s (a) $\frac{di}{dt}$ gradients (b) Output voltages, and (c) Output currents. [Blue → Converter-1, Red→ Converter-2, Yellow→ Bi-directional Converter, and Green→ Load Current]

Fig. 15 illustrates the fault detection and isolation of a line-line fault with R_f=10 Ω. The calculated $\frac{di}{dt}$ gradient for bus#1 converters are shown Fig. 15(a). The converters output voltage is presented in Fig. 15(b). As shown in the Fig. 15(c), due to the fault, the converter-1 output current magnitude rises to 6 A. At 0.02059 s, the trip signal is generated based on the changes in the current direction at the bus side IED_1. The total trip time is measured as 590 μs as shown in the Fig. 15(c).

2) Feeder Fault (F_2): At 0.025 s, a low impedance line-line fault (F2) with R_f=1 Ω is initiated, and the simulation result is presented in Fig. 16. The IED_{12} and IED_{21} isolates the feeder from the system as soon as the current direction changes, and peak bus current is observed as 4 A as shown in Fig. 16(b). Fig. 17 illustrates the bus#1 converter's performance during the fault, and it indicates that the fault does not affected the smooth operation of the converters.

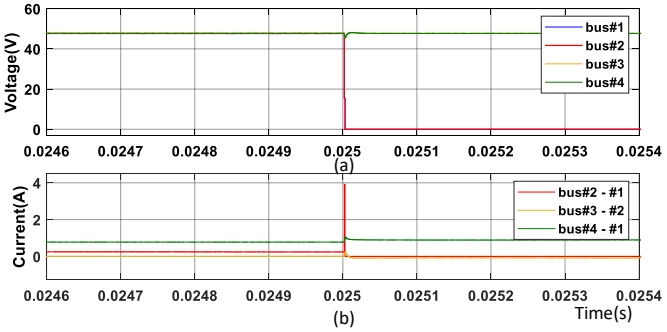

Fig. 16. Results for a low impedance line-line feeder fault F_2 at 0.025 s (a) Bus voltages, and (b) Bus currents.

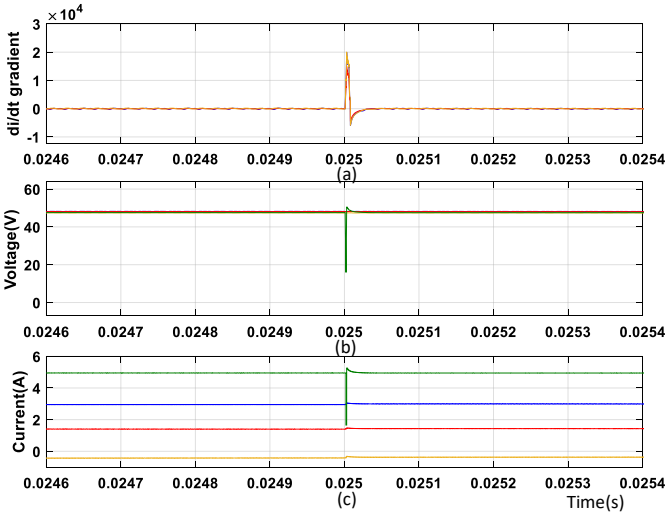

Fig. 17. Results for converter's at bus#1 for a low impedance line-line feeder fault F_2 at 0.025 s (a) $\frac{di}{dt}$ gradients (b) Output voltages, and (c) Output currents. [Blue → Converter-1, Red→ Converter-2, Yellow→ Bi-directional Converter, and Green→ Load Current]

B. High Impedance Fault

1) Converter-1 - Bus#1 Cable Fault (F_3): The impact of a high impedance line-ground fault (F_3) with R_f=500 Ω is also tested to validate the performance of the proposed method, and the results are shown in Fig. 18. The fault signal is activated at 0.02 s. In this case, the differential current comparison is used, and a flag is activated with a current difference threshold of 50 mA. The corresponding trip signal is generated after a preselected delay of 1 ms. The delay is provided to make sure the high impedance fault is not temporary. If the fault persists after the delay, then a trip signal is sent to the IED.

2) Feeder Fault (F_4): Fig. 19 shows the result of a high impedance line-ground feeder fault (F_4) with R_f=500 Ω. In this scenario, the fault signal is activated at 0.025 s. Based on the differential current comparison, and 1 ms delay, a trip signal is sent to IED_{12} and IED_{21} at 0.026 s to isolate the feeder. Fig. 20 shows the bus#1 converter's performance during the fault. The $\frac{di}{dt}$ gradients which are less than the threshold are shown in Fig. 20(a). This indicates that, the converters operates steadily during a high impedance feeder fault.

C. Line-Line and Line-Ground Faults at Bus#1 Converters

As shown in Fig. 21, a low impedance line-line fault at converter-1 at 0.015 s, and a high impedance line-ground fault at converter-2 at 0.020 s is created to analyze the system performance. From Fig. 21(a), it is clear that, the magnitude of $\frac{di}{dt}$ gradients are different for the type of fault, and fault impedance. The corresponding voltage and current waveforms are presented in Fig. 21(b, c) respectively. The converter-2 high impedance fault is isolated at 0.021 s after a delay of 1 ms. Fig. 22(a, b) show the bus voltages and currents during this scenario. The bus#4 is supplying a current of 3.2 A to the bus#1's load.

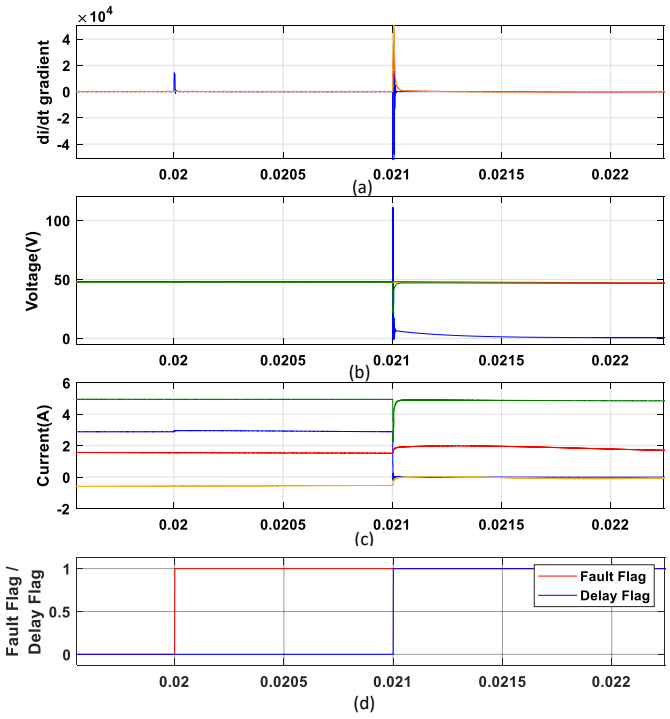

Fig. 18. Results for converter's at bus#1 for a high impedance cable fault F_3 at 0.02 s (a) $\frac{di}{dt}$ gradients (b) Output voltages (c) Output currents, and (d) Current direction/delay flag. [Blue → Converter-1, Red→ Converter-2, Yellow→ Bi-directional Converter, and Green→ Load Current]

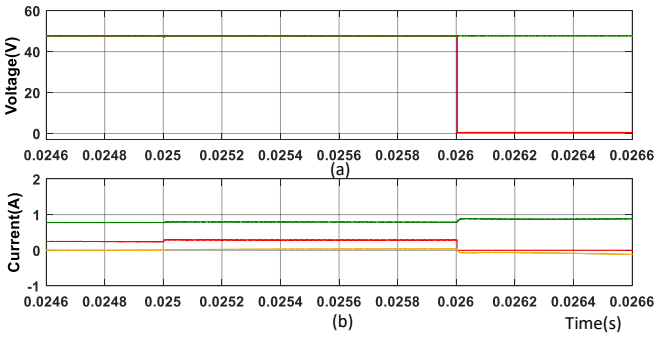

Fig. 19. Results for high impedance feeder fault F_3 at 0.025 s (a) Bus voltages, and (b) Bus currents.

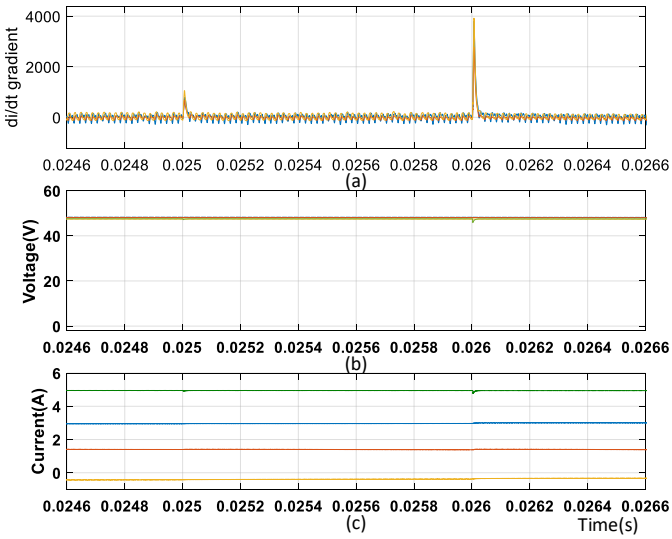

Fig. 20. Results for high impedance feeder fault F_3 at 0.025 s (a) $\frac{di}{dt}$ gradients (b) Output voltages, and (c) Output currents. [Blue → Converter-1, Red→ Converter-2, Yellow→ Bi-directional Converter, and Green→ Load Current]

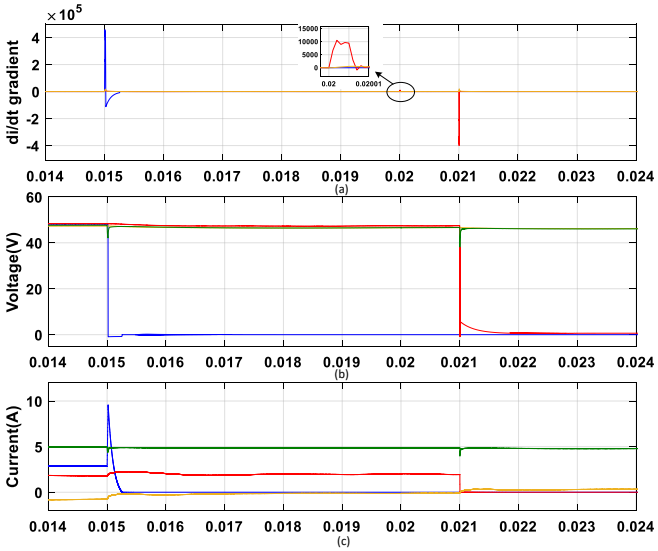

Fig. 21. Simulation results for a combined line-line and line-ground faults at bus#1 Converter's(a) $\frac{di}{dt}$ gradients (b) Output voltages, and (c) Output currents. [Blue → Converter-1, Red→ Converter-2, Yellow→ Bi-directional Converter, and Green→ Load Current]

D. Load Change

The performance of the proposed control algorithm is tested for a step change in current from 3 A to 8 A in bus#1 load as shown in Fig. 23. It can be observed that, all converters are stable and operating smoothly during the large load transient irrespective of the $\frac{di}{dt}$.

Based on the simulation results summarized in Table IV, it can be concluded that, the proposed scheme can effectively detect a system event based on the $\frac{di}{dt}_{(th)}$, and classify the event using directional and differential comparison. This will help to isolate the converter or a part of the DC microgrid system in minimum time bound.

TABLE IV
RESULT ANALYSIS

Fault/Load Change	**Fault Clearing Time (s)**	$\frac{di}{dt}$ **(A/s)** (measured)
Low impedance fault (without $\frac{di}{dt}$ and droop)	205μs	-
Low impedance fault (1Ω) (with $\frac{di}{dt}$ and droop)	265 μs	4×10^5 A/s
Low impedance fault (10Ω) (with $\frac{di}{dt}$ and current direction)	590 μs	3×10^5 A/s
High impedance fault (500 Ω) (with $\frac{di}{dt}$ and current differential)	1 ms (pre-selected)	$1.5times10^4$ A/s
Small load change (3 A to 4 A)	-	1×10^4 A/s
Large load change (3 A to 8 A)	-	7×10^4 A/s

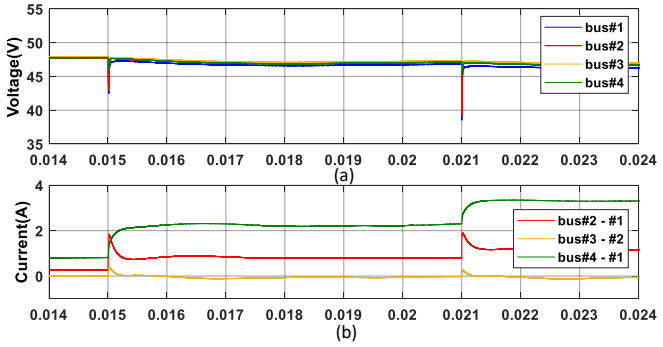

Fig. 22. Simulation results for combined line-line and line-ground faults at bus#1 Converter's (a) Bus voltages, and (b) Bus currents.

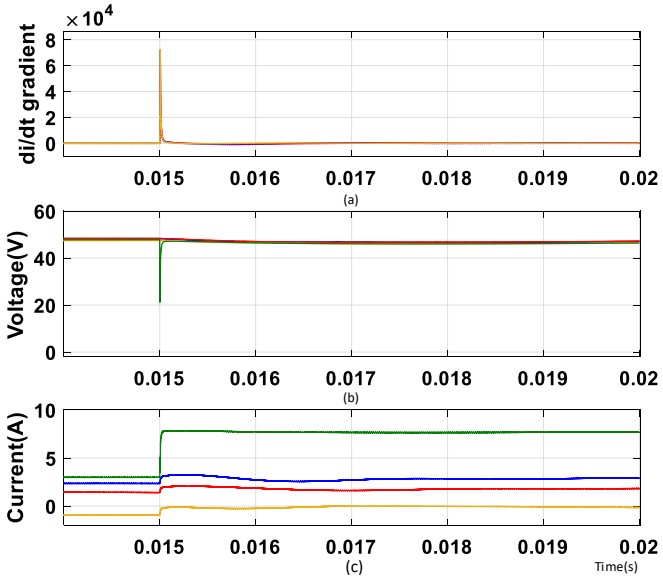

Fig. 23. Simulation results for a step change in bus#1 load at 0.025 s (a) $\frac{di}{dt}$ gradients (b) Output voltages (c) Output currents, and (d) Current direction / difference flags. [Blue → Converter-1, Red→ Converter-2, Yellow→ Bi-directional Converter, and Green→ Load Current]

V. Conclusion

Implementing a good protection scheme for islanded DC microgrids is a major task to guarantee the seamless power flow during faults, or disturbances. In this paper, a combination of current derivative, adaptive droop current directional and differential comparison scheme with an improved DC microgrid fault characterization algorithm is proposed. After locating a fault, the method effectively characterize it as L-L, L-G, or a disturbance in the system. From the results it is found that the proposed algorithm gives an additional time of 60 μs to clear a low impedance fault. Also, during a high impedance fault condition, the proposed method isolates the fault within 1 ms. It is also shown that the proposed technique can easily classify a large load disturbances and a fault, which is very important feature to facilitate the smooth operation of a DC microgrid. To improve the performance and reliability of a large scale DC microgrid system the future work should effectively incorporate the fault distance measurement algorithm and study the behavior of the virtual inertia control during a fault. The effectiveness of system with the centralized controller need to be investigated further. Also, the performance of the proposed method needs to be tested on grid connected mode.

Acknowledgment

The authors would like to gratefully acknowledge support for this work from Sandia National Laboratories. Sandia National Laboratories is a multimission laboratory managed and operated by National Technology & Engineering Solutions of Sandia, LLC, a wholly owned subsidiary of Honeywell International Inc., for the U.S. Department of Energys Na-tional Nuclear Security Administration under contract DE-NA0003525. This paper describes objective technical results and analysis. Any subjective views or opinions that might be expressed in the paper do not necessarily represent the views of the U.S. Department of Energy or the United States Government.

References

[1] T. Dragicevic, J. Vasquez, J. Guerrero, and D. Skrlec, "Advanced LVDC electrical power architectures and microgrids: A step toward a new generation of power distribution networks." *IEEE, Electri. Mag.*, vol. 2, no. 1, pp. 54–65, Mar. 2014.

[2] S. Kotra and M. K. Mishra, "Design and stability analysis of DC microgrid with hybrid energy storage system," *IEEE Transactions on Sustainable Energy*, vol. 10, no. 3, pp. 1603–1612, July 2019.

[3] V. Nasirian, S. Moayedi, A. Davoudi, and F. Lewis, "Distributed cooperative control of DC microgrids," *IEEE Trans. Power Electron.*, vol. 30, no. 4, pp. 2288–2303, Apr. 2015.

[4] S. Beheshtaein, R. M. Cuzner, M. Forouzesh, M. Savaghebi, and J. M. Guerrero, "DC microgrid protection: A comprehensive review," *IEEE Journal of Eme. and Sele. Topics in Power Elect.*, pp. 1–1, 2019.

[5] D. M. Bui, S. Chen, C. Wu, K. Lien, C. Huang, and K. Jen, "Review on protection coordination strategies and development of an effective protection coordination system for DC microgrid," in *IEEE PES Asia-Pacific Power and Energy Eng. Conf. (APPEEC)*, Dec 2014, pp. 1–10.

[6] D. S. Pillai and N. Rajasekar, "A comprehensive review on protection challenges and fault diagnosis in pv systems," *Renewable and Sustainable Energy Reviews*, vol. 91, pp. 18 – 40, 2018.

[7] S. Beheshtaein, R. Cuzner, M. Savaghebi, and J. M. Guerrero, "Review on microgrids protection," *IET Gen., Trans. Distri.*, vol. 13, no. 6, pp. 743–759, 2019.

[8] S. Augustine, J. E. Quiroz, M. J. Reno, and S. Brahma, "DC microgrid protection: Review and challenges," in *Sandia National Laboratories, SAND2018-8853, 2018.*

[9] D. S. Pillai and R. Natarajan, "A compatibility analysis on NEC, IEC, and UL standards for protection against Line-Line and Line-Ground faults in PV arrays," *IEEE Journal of Photovoltaics*, vol. 9, no. 3, pp. 864–871, May 2019.

[10] T. R. de Oliveira, A. S. Bolzon, and P. F. Donoso-Garcia, "Grounding and safety considerations for residential DC microgrids," in *40th Annual Conf. of the IEEE Ind. Elect. Society*, Oct 2014, pp. 5526–5532.

[11] M. Mobarrez, D. Fregosi, S. Bhattacharya, and M. A. Bahmani, "Grounding architectures for enabling ground fault ride-through capability in DC microgrids," in *IEEE Second Intern. Conf. on DC Microgrids (ICDCM)*, June 2017, pp. 81–87.

[12] S. Augustine, S. M. Brahma, and M. J. Reno, "Fault current control for DC microgrid protection using an adaptive droop," in *IEEE 28th International Symp. on Ind. Elect. (ISIE)*, June 2019, pp. 2591–2596.

[13] J. Park, J. Candelaria, L. Ma, and K. Dunn, "DC ring-bus microgrid fault protection and identification of fault location," *IEEE Trans. on Power Deli.*, vol. 28, no. 4, pp. 2574–2584, Oct 2013.

[14] S. D. A. Fletcher, P. J. Norman, S. Galloway, and G. Burt, "Fault detection and location in DC systems from initial di/dt measurement," 2012.

[15] X. Feng, Q. Xiong, D. Wardell, A. L. Gattozzi, S. M. Strank, and R. E. Hebner, "Extra-fast DC distribution system protection for future energy systems," *IEEE Trans. on Ind. Appli.*, vol. 55, no. 4, pp. 3421–3430, July 2019.

[16] J. Park and J. Candelaria, "Fault detection and isolation in low-voltage DC-bus microgrid system," *IEEE Trans. on Power Deli.*, vol. 28, no. 2, pp. 779–787, April 2013.

[17] S. Dhar, R. K. Patnaik, and P. K. Dash, "Fault detection and location of photovoltaic based DC microgrid using differential protection strategy," *IEEE Trans. on Smart Grid*, vol. 9, no. 5, pp. 4303–4312, Sept 2018.

[18] C. Yuan, M. A. Haj-ahmed, and M. S. Illindala, "Protection strategies for medium-voltage direct-current microgrid at a remote area mine site," *IEEE Trans. on Ind. Appli.*, vol. 51, no. 4, pp. 2846–2853, July 2015.

[19] L. Zhang, N. Tai, W. Huang, J. Liu, and Y. Wang, "A review on protection of DC microgrids," *Journal of Modern Power Syst. and Clean Energy*, vol. 6, no. 6, pp. 1113–1127, Nov 2018.

[20] E. Christopher, M. Sumner, D. W. P. Thomas, X. Wang, and F. de Wildt, "Fault location in a zonal DC marine power system using active impedance estimation," *IEEE Trans. on Ind. Appli.*, vol. 49, no. 2, pp. 860–865, March 2013.

[21] D. Thomas, M. Sumner, D. Coggins, X. Wang, J. Wang, and R. Geertsma, "Fault location for DC marine power systems," in *IEEE Electric Ship Tech. Symp.*, April 2009, pp. 456–460.

[22] R. Mohanty, U. S. M. Balaji, and A. K. Pradhan, "An accurate non-iterative fault-location technique for low-voltage DC microgrid," *IEEE Trans. on Power Deli.*, vol. 31, no. 2, pp. 475–481, April 2016.

[23] J. Wang, B. Berggren, K. Linden, J. Pan, and R. Nuqui, "Multi-terminal DC system line protection requirement and high speed protection solutions," *CIGRE International Symposium*, pp. 1–9, 2015.

[24] M. Reis, "Optimization of dc feeder rate of rise overcurrent protection settings using delta i cumulative distribution," in *IEEE Indu. and Commercial Power Sys. Tech.*, May 2004, pp. 63–66.

[25] R. M. Cuzner, K. Palaniappan, W. Sedano, N. Hoeft, and M. Qi, "Fault characterization and protective system design for a residential DC microgrid," in *IEEE 6th Int.l Conf. on Renewable Energy Research and Appli. (ICRERA)*, Nov 2017, pp. 642–647.

[26] S. D. A. Fletcher, P. J. Norman, K. Fong, S. J. Galloway, and G. M. Burt, "High-speed differential protection for smart DC distribution systems," *IEEE Trans. on Smart Grid*, vol. 5, no. 5, pp. 2610–2617, Sep. 2014.

[27] S. Augustine, M. K. Mishra, and N. Lakshminarasamma, "A unified control scheme for a standalone solar-PV LVDC microgrid system with HESS," *IEEE Journal of Eme. and Sele. Topics in Power Elect.*, pp. 1–1, 2019.

Sijo Augustine (S'13-M'17) received the AMIE degree in Electrical Engineering from Institution of Engineers [India] in 2008, M.Tech in Power Electronic and Drives from VIT University, Vellore, India in 2010 and Ph.D. degree in Electrical Engineering from Indian Institute of Technology Madras, Chennai, India in 2016. He is currently working as a post-doctoral research scientist at New Mexico State University, USA. His research interests includes power electronics, DC/AC/Hybrid microgrids and energy management.

Matthew J. Reno (M'09-SM'19) is a Principal Member of Technical Staff in the Electric Power Systems Research Department at Sandia National Laboratories. His research focuses on distribution system modelling and analysis with high penetration PV, including advanced software tools for automated analysis of hosting capacity, PV interconnection studies, and rapid Quasi-Static Time Series simulations. Matthew is also involved with the IEEE Power System Relaying Committee for developing guides and standards for protection of microgrids and systems with high penetrations of inverter-based resources. He received his Ph.D. in electrical engineering from Georgia Institute of Technology and has been at Sandia for the last 10 years.

Sukumar Brahma received the B.Tech. degree from Gujarat University, the M.Tech. degree from the Indian Institute of Technology, Bombay, and the Ph.D. degree from Clemson University, Clemson, USA, in 2003, all in electrical engineering. He is the Dominion Energy Distinguished Professor in Power Engineering and the Director of Clemson University Electric Power Research Association at Clemson University. Before joining Clemson, he was the William Kersting Endowed Chair Professor with New Mexico State University, USA. His research, funded by diverse sources, has focused on different aspects of power system modeling, analysis, and protection.

Dr. Brahma has chaired IEEE PES Distribution System Analysis Subcommittee and Power and Energy Education Committee. He is a member of the Power System Relaying Committee, where he has been contributing to and leading working groups that produce reports, guides, and standards in the area of power system protection. He is an Editor for the IEEE Transactions on Power Delivery and served as the Guest Editor-in-Chief for the Special Issue on Frontiers of Power System Protection for the journal. He is a Distinguished Lecturer and Fellow of the IEEE.

Olga Lavrova (SM 2000, M 2011) is Associate Professor at the Electrical and Computer Engineering Department at the Klipsch School of Electrical and Computer Engineering at the New Mexico State University. Prior to that, Dr. Lavrova was a Principal Member of Technical Staff at Sandia National Labs in the Photovoltaics and Distributed Systems Integration Department. Prior to that, she held position of Assistant Professor at the Electrical and Computer Engineering Department at the University of New Mexico.

She received her B.Sc. degree in Physics and M.Sc. degree in EE from the St.Petersburg State Electrical Engineering University, and her Ph.D. degree from UCSB in 2001. Her current work and areas of interest include photovoltaics and nano-scale semiconductor structures for photovoltaic applications, Smart grids, Renewable Energy, Controls of electric grid, smart grids and renewable energy integration, electric storage systems and power electronics.